# Spherical Images and Inextensible Curved Folding

Keith A. Seffen

kas14@cam.ac.uk

Advanced Structures Group Laboratory, Department of Engineering, University of Cambridge, UK, CB2 1PZ

December 14, 2017

**Abstract**

In their study from 1982, Duncan and Duncan [1] calculate the shape of an inextensible surface folded in two about a general curve. They find the analytical relationships between pairs of generators linked across the fold curve, the shape of the original path, and the fold angle variation along it. They present two special cases of generator layouts for which the fold angle is uniform or the folded curve remains planar, for simplifying practical folding in sheet-metal processes. We verify their special cases by a graphical treatment according to a method of Gauss. We replace the fold curve by a piece-wise linear path which connects vertices of intersecting pairs of hinge lines. Inspired by the "d-Cone" analysis in [2], we construct the spherical images for developable folding of successive vertices: the operating conditions of the special cases in [1] are then revealed straightforwardly by the geometric relationships between the images. Our approach may be used to synthesise folding patterns for novel deployable and shape-changing surfaces without need of complex calculation.

## 1 Introduction

In their paper, "Folded Developables", Duncan and Duncan [1] present an elegant treatise of the shape acquired by an inextensible sheet after it is folded about a general internal planar curve. They approach matters by first modifying the Serret-Frenet coupled differential equations for the curvature and torsion of a general space curve to read in terms of the orthogonal components of geodesic and normal curvatures. The geodesic component describes the original, planar layout of the curve before folding, and is a fixed property whilst the normal component correlates to the current surface curvature in a tangential direction to the folded curve. Meusnier's Theorem formally relates these curvatures to the fold angle and ultimately to the spatial torsion of the fold curve, the corresponding adjacent geodesic torsion in the edge of the connecting surface, and to the rate of change of fold angle along the curve after a theorem from Bonnet. The rules for compatible folding between surfaces on either side of the folded curve are set by assuming that at any common point along it, they have equal and opposite tangential curvatures and make equal fold angles to the local dihedral plane; the relationship between the geodesic torsions and the intrinsic variation of the fold angle along the curve then follows.

Duncan and Duncan illustrate two degenerate cases informed by their research experiences of sheet-metal working: first, where the folded curve forms a planar ridge and, second, where the fold angle is the same everywhere, see Fig. 1. These conditions are usually mutually exclusive, with a varying fold angle in the first case and the folded curve moving out of plane in the second. For each of these cases, Duncan and Duncan calculate the geodesic torsion of the surfaces

at any common fold point to be equal and opposite or equal to each other, respectively. Since the tangential curvatures are also known, the developable geometries of both sets of surfaces are completely specified, where a Mohr's circle construction reveals the corresponding directions of pairs of generators linked together across the fold curve. These directions do not change during folding owing to the intrinsic nature of the Mohr's circle and, hence, are most simply expressed in "planar" development—before folding occurs. For the first case, Duncan and Duncan show that linked generators are collinear, and in the second, the generators are equally inclined to the local tangent of the fold curve. The latter has a planar optics analogy if we imagine the fold curve to be a reflective surface where an incident light ray replaces either generator; the reflected ray extrapolated backwards through the curve yields the direction of the other generator. In both cases, the curvatures of the linked generators are equal and opposite, giving locally convex and concave surfaces, see Fig. 1.

We verify these special generator conditions using a graphical construction first proposed by Gauss [3], which emerges as a special case from his famous *Theorema Egregium* of deforming surfaces. Apart from extolling the potency and elegance of his theorem, our approach is intimately connected to sheet folding in a general way and may apply to the synthesis, design and performance of novel deployable, shape-changing and "origami"-based structures with curved folds, as reported in [4, 5, 6, 7]. Our approach also differs from others in capturing the deformed shape by geometrical means alone; elsewhere, the folded curve is treated as a varying geometrical constraint on the developable shape of the connected sheets either side, where both are quantified from minimising the stored strain energy of deformation. In this regard, the folding response of the fold curve itself is required along with the elastic bending energy of the sheets. Our approaches together, we believe, would converge if the curve were to fold freely whilst obliging the particular folding conditions of Duncan and Duncan: and this may prove a useful comparison for future studying. Notwithstanding, we offer an alternative, graphical method based on rules of construction rather than solving differential equations of shape, which may appeal to the readership. Understanding the detailed mechanics of creasing and fold formation is a separate issue, with recent strides available in, for example, [8, 9].

Inspired by the heavily scored sheet-metal examples to produce discrete bending in [1], we approximate the deformed shape by rigid facets folding about singular hinge lines. The fold curve must be rendered piece-wise linear between the junctions of linked hinge lines performing as "discrete" generators, which altogether form as shallow vertices along the curve, each with four intersecting hinge lines. A higher density of hinge lines brings us closer to smooth surface curving made of pure generators but this is not essential here.

We apply Gauss's construction to the facet inclinations around each vertex, which gives the relationship between the hinge line rotations for developable folding. This method was originally used by Farmer and Calladine [2] to study the buckled geometry of a familiar conical defect, or "d-Cone", in a thin plate deforming sharply and asymmetrically underneath a point load, Fig. 1. In their first model, they captured the overall proportions of d-Cone using a straightforward but effective vertex of five intersecting hinge lines. They increased the hinge detail by dividing the d-Cone into discrete conical and cylindrical surfaces about a parabolic crease. They proceeded to calculate hinge line rotations iteratively from properties of their earlier single vertex and, in an earlier example, they confirmed explicitly a planar folded crease for a partially inverted cylinder whose generator layout conforms to the first special case in [1]. They were not aware of Duncan and Duncan's work at the time but they clearly had an excellent intuitive grasp of performance expressed in bespoke examples. We aim to extend their work in a general way: first, we introduce our method for the simplest possible d-Cone vertex; we then propose hinge layouts for each of the two cases in [1] whose surface properties are evidently expressed in the relationship between successive vertices moving along the fold curve,

before finishing off with an example of a detailed d-Cone.

## 2 Gauss Mapping

The simplest developable cone, or d-Cone, forms when a central point force is impressed upon a rim-supported thin plate, see Fig. 2(a). The rim and plate are circular, and a buckled portion lifts off the rim against the load direction to give two distinctly curved regions in opposite senses. The simplest rigid-body folding analogue is shown in Fig. 2(b), of four facets (A, B, C, D) separated by three "valley" hinge lines and one "mountain" hinge running along the buckled apex. The original layout in plan-view is symmetrical with two of the valley hinges inclined at acute angles, $\alpha$, to the mountain one. Three points on the boundary (P, Q, R) remain in contact with the rim during loading, and the hinge lines rotate and move out of plane.

The relative rotation between adjacent facets can be correlated to the change in orientation of unit vectors appointed normally to their surfaces, Fig. 2(c), according to a method of Gauss [3]. The normals are identically mapped onto the surface of a sphere of unit radius, Fig. 2(d), thereby defining the "location" of folded facets as unique points: moving across a hinge line, we move from one facet to the next, tracing out a great arc on the sphere, which is precisely the relative rotation angle between the facets. When the vertex is encircled completely, moving from facet A to B *etc* back to A, we obtain the outline of a closed figure called the *spherical image*; and in his famous theorem, Gauss equates the spherical surface area to the solid angle subtended by the vertex. In Fig. 2, the image is a distinctive bow-tie because its "parallel" sides of valley and mountain hinges are in opposite senses.

Farmer and Calladine [2] set the bow-tie area equal to zero for inextensible folding of the vertex within the original flat sheet which has zero solid angle. For non-trivial solutions, the area must have substance *i.e.* its portions must be of opposite "sign" in order they sum to zero. The areal sign can be defined by the right- or left-handedness of the path enclosing its various parts. The image in Fig. 2(d) has two similar spherical triangles of opposite enclosure, which must be equal in magnitude: a view directly above the cross-over point in Fig. 2(e) shows this requirement more clearly. If any side-length increases or decreases, signifying a change in rotation angle of that hinge line, the image simply scales congruently over the surface of the sphere (for $\alpha$ fixed). All rotations are thence related to each other but calculating their absolute values from spherical geometry is not trivial and rarely yields compact expressions. Farmer and Calladine assumed that the d-Cone shape is set in early deformation when gradients are small, giving equivalent hinge line rotations no more than 15°; consequently, the planar projection of the spherical image is virtually unchanged and has a simpler area calculation. They also noted that the planar image can be reconstructed straightforwardly by adding the rotation vectors along hinge lines nose-to-tail as we move around the vertex. The image is the same except for a right-angled rotation in plan compared to that on the unit sphere, see Fig. 2(f). We shall construct images the same way.

We also note that the valley hinge lines next to the mountain remain co-planar during folding. Symmetry implies this outright but it be can formally construed from the original spherical image of Fig. 2(d). If we replace the mountain hinge and the facets C and D by a single planar wedge between the valley hinges and denoted as E, Fig. 2(g), the new spherical image must have three sides but retain the original contributions from facets A and B as well as from the original valley lines. The same is found by deleting one half of the original image below the junction of their great arcs, Fig. 2(h), which now locates the normal to the new wedge facet. The pre-requisite for co-planarity of any pair, or set, of hinge lines is thus a shared intersection point, which is also true for the planar approximated image.

This single vertex performance enables us now to tackle the special cases of Duncan and Duncan. We substitute continuum generator layouts with discrete hinge lines of the same nominal pattern. Pairs of hinges are also linked across the original fold curve, now forming as straight hinge lines between the junctions of each pair; these junctions are the locations of developable vertices. The shape of the folded sheet now resembles a series of bent and narrow strips, becoming a more accurate version of the continuum case as the hinge density increases. The conditions for the special cases do not depend on the number of hinge lines but it is imprudent to assume that the fold curve location of vertices can be, likewise, arbitrarily specified. For the first special case, it does not matter because the linked hinges are collinear, but the optics analogy of the second imputes a location requirement between successive vertices for developable folding, as will shall see.

Henceforth, we use "hinge" exclusively for describing the linked generators they replace and "fold" for the original fold curve, even though both are sets of hinge lines. We shall employ small rotations to extract rotations in closed form; the supporting geometrical arguments are equally applicable for large rotations but we do not give an explicit proof.

# 3 Special Cases

*Case I*

Pairs of collinear hinge lines, their vertices and the linearised fold path between them are shown in planar development in Fig. 3(a). The locus of the original fold curve is general but we show one that is singly curved for simplicity. Facets are labelled $C_1$, $C_2$ *etc* on the concave side, and $D_1$, $D_2$ ... convex; "1", "2" ... are the nodal labels of the vertices arbitrarily spaced along the fold. Vertex 1 is surrounded anticlockwise by the four facets, $C_1$, $D_1$, $D_2$ and $C_2$, and two angles, $\theta_{c1}$ and $\theta_{d1}$, specify its layout. The four rotation vectors must observe the same developable folding rules as the earlier d-Cone where, if we assume that the folding is always uni-directional along the fold curve, the rotation vector of the generator on the acute *i.e.* concave side is of opposite sign to the rest and is drawn dashed as shown. Labelling these rotations as $\beta_{c1}$ and $\beta_{d1}$ for the hinge lines, and $\beta_1$ and $\beta_2$ for the fold line segments, we then add these vectors nose-to-tail moving around the vertex under the same sign convention as before.

The planar spherical image in Fig. 3(b) is generally a slender antisymmetrical bow-tie where the central scissor angle, $\theta_{d1} - \theta_{c1}$, is typically small. Since $\beta_{c1}$ and $\beta_{d1}$ are parallel, the upper and lower triangles are similar, and their areas balance when $\beta_1$ and $\beta_2$ cross over exactly halfway along with $\beta_{c1}$ equal to $\beta_{d1}$ in opposite directions. The fold lines are co-planar *c.f.* Fig. 2(h) and $\beta_1 \sin\theta_{c1} = \beta_2 \sin\theta_{d1}$, giving, in general, a *change* in fold rotation across the vertex.

The image for vertex 2 is similarly constructed in Fig. 3(c), where the labelling scheme has been extended with vectors $\beta_{c2}$ and $\beta_{d2}$ for hinge line rotations, and $\beta_3$ for the fold line rotation to vertex 3. The cross-over point is again halfway along $\beta_2$ and $\beta_3$, and because $\beta_2$ is common to both vertices 1 and 2, the images can be superposed. They clearly share the same cross-over point, as would subsequent vertex images if drawn, and all fold lines must therefore lie in a single plane after folding takes place. If we assume the hinge rotations to be averaged over the facet widths between them, we have an equivalent statement about the local surface curvatures they purport to capture, which also matches the continuum curvature results in [1]. The rate of change of rotations obviously depends on the spacing between vertices and on the fold locus, but for elemental changes across the vertex where $\beta_2 = \beta_1 + \delta\beta_1$ and $\theta_{d1} = \theta_{c1} + \delta\theta_{c1}$, we can write:

$$\beta_1 \sin\theta_{c1} = (\beta_1 + \delta\beta_1)\sin(\theta_{c1} + \delta\theta_{c1}) \quad \rightarrow \quad \delta\beta_1 \sin\theta_{c1} + \beta_1 \cos\theta_{c1}\delta\theta_{c1} = 0$$

We cannot strictly observe the limit because this conflicts with our discrete scheme: all vertices would merge together onto the fold curve and the scissor angle of each spherical image becomes zero, leading to a meaningless area interpretation. But we have an equivalent continuum statement that can be compared to Duncan and Duncan's result where, dividing by $\delta\theta_{c1}$, omitting the subscripts for generality's sake, the equation governing the fold angle and path shape is found as:

$$\frac{\mathrm{d}\beta}{\mathrm{d}\theta} = -\beta\cot\theta \quad \rightarrow \quad \beta\sin\theta = \text{constant}$$

The fold angle cannot be constant if $\theta$ varies, as it must do for a fold curve other than being straight. This matches the claim in [1].

*Case II*

Pairs of linked hinge lines are equally inclined to the fold tangent and do not intersect other pairs away from their vertices. We specify, however, parallel hinges on one side of the fold for marginal graphical simplicity compared to a general description, which follows without a formal analysis. The labelling scheme is the same as Case I with parallel hinges meeting the concave side of the fold before turning through some angle $2\gamma_1$, $2\gamma_2$ ... on the convex side at vertex 1, 2 ..., see Fig. 4(a). Each $\gamma$ is the angle made by each hinge line pair to the local tangent of the original fold curve, being slightly different to each pair of $\theta$ angles associated with its piece-wise approximation. We see this difference clearly in Fig. 4(b) for vertex 1 where we measure the inclination of the fold line pair by $\theta_{c1}$ and $\theta_{d1}$ relative to the concave-side hinge line. The corresponding Gauss mapping is shown in Fig. 4(c), where internal angles, $x$ and $y$ are highlighted. When the lines of each rotation vector, $\beta_{c1}$ and $\beta_{d1}$, are extrapolated to their intersection, we can verify their relative inclination as $\pi - 2\gamma_1$; from this, we find $x = \pi - \theta_{d1} - (\pi - 2\gamma_1) = 2\gamma_1 - \theta_{d1}$, and $y$ is simply $\theta_{d1} - \theta_{c1}$. The upper and lower triangles are identical for zero net area which enforces $x = \theta_{c1}$ *i.e.* $2\gamma_1 = \theta_{d1} + \theta_{c1}$ or:

$$\gamma_1 - \theta_{c1} = \theta_{d1} - \gamma_1 \quad (= z_1, \text{ say.}) \tag{1}$$

Fold line segments at a given vertex are thus equally inclined to the tangent of the original fold curve by an angle $z_1$, see Fig. 4(b). Ascribing the optics analogy therefore dictates the location of vertices relative to the first vertex—unlike Case I vertices. The intersection of the fold line from vertex 1 with the original fold curve determines the position of the second vertex; at this point, the direction of the concave-side hinge line sets the tangent angle, $\gamma_2$, and hence $z_2$, the convex hinge direction and ultimately the direction of the fold path to vertex 3, and so forth. As the number of vertices increases, the difference between $\gamma$ and $\theta$ angles diminishes, and the fold line segments tend towards the local tangent. As noted for Case I, we cannot flout our discrete scheme by observing the limit, but it rightly shows our performance expectation converging towards the continuum case.

The spherical image of vertex 1 is symmetrical and yields equal fold rotations, $\beta_1$ and $\beta_2$, as well as equal and opposite hinge line rotations. After locating vertex 2, we construct its spherical image, which also shares $\beta_2$, see Fig. 4(d). Symmetry ensures zero net area with $\beta_3 = \beta_2$ (fold lines) and $\beta_{c2} = -\beta_{d2}$ (hinges) but where the cross-over point is different compared to vertex 1. The fold angle is conserved between vertices, the linked hinge rotations across

the fold are the same at a given vertex, but the fold line segments do not share the same plane, all of which match the claims made by Duncan and Duncan. A final third image in Fig. 4(e) trivially shows the last rule.

If we relax the parallel condition, these rules are obeyed for many arrangements of "incoming" (dashed) hinges and fold path shape. Moving from vertex to vertex in a formal analysis, we define the relative inclinations of the fold line segments to the incoming hinge as in Fig. 4 before operating upon the spherical image: but the outcome is the same, so we do not need to. Figure 5, however, indicates when also to expect planarity of fold lines between a pair of vertices for this case.

The first spherical image is symmetrical where each of the two larger fold line rotations has been split into two smaller vectors, $m$ and $n$, Fig. 5(a). The image for the next vertex comprises one of their fold rotation vectors and a new one of the same size also split into $m$ and $n$ about the same cross-over point but inclined at some arbitrary angle to the first, see Fig. 5(b); when the hinge line rotations are now added for completeness, the second image is automatically symmetrical. Figure 5(c) then shows the corresponding fold path and hinge layout for some declared spacing between vertices, which gently undulates in this example with the dashed hinges swapping sides. If the linked hinges happen also to be parallel, the rules for Cases I and II apply together, for example, when hinge lines are normal to a circular fold path, Fig. 5(d), resulting in uniformly curved, opposite conical surfaces, which is declared in [1].

# 4 D-Cone

We return to the d-Cone shape of Farmer and Calladine [2] in Fig. 6: recall the set-up from Fig. 1(c). They observed from experiments and finite element studies that the rising buckle was largely cylindrical, surrounded by a conical impression, and separated by a narrow transition region of approximately parabolic outlay. They reasoned a parabola from what is known about intersecting conic sections and from the simpler inextensible behaviour of an indented open cylinder; close examination by others *e.g.* Cerda and Mahadevan [10], Chaieb and Melo [11] and Liang and Witten [12] of the loading region also confirms a local and sharp plastic parabolic crease. Extending its profile to the outer edge for a complete parabolic fold curve is, of course, an approximation but is fair in view of the small transition width found in experiments in [10]. At higher deformation gradients, which lie outside of the scope of this study, the fold curve is more accurately described as being hyperbolic than parabolic, see [11]. The parabola in [2] subtends an angular width of 90° at the rim, which we maintain here.

Our hinge line pattern is generically the same in Fig. 6(a) with conical-section hinge lines extrapolating to the focus of the parabolic fold as per Case II rules. The cylindrical-section hinges are aligned to the $y$ direction of an $(x, y)$ coordinate system originating from the centre of the fold. Its shape is thus described by $y = -x^2/4a$, where $(0, -a)$ locates the focus generally; when the buckle width subtends angle $2\alpha$ at the rim of radius $R$, Fig. 6(a), we can show:

$$\frac{\sin^2\alpha}{\cos\alpha} = \frac{a}{R} \quad (= 1/4\sqrt{2} = 0.177 \text{ for } 2\alpha = 90^\circ) \tag{2}$$

The pattern is symmetrical about $y$ and the first pair of collinear hinges are drawn in this direction through the first vertex at the disk centre, $(x_1, y_1) = (0, 0)$, to meet the rim. Another cylindrical hinge is then drawn at a small separation along $x$, giving a second vertex where it meets the parabola at $(x_2, y_2)$; the inclination of the tangent to the hinge line, $\gamma$, is found from:

$$\gamma = \pi/2 - \arctan|\mathrm{d}y/\mathrm{d}x| \quad \rightarrow \quad \gamma_1 = \pi/2 - \arctan(x_1/2a)$$

which enables the conical-section hinge to be drawn on the other side inclined at the same angle. We draw the fold line segment from the disk centre to this vertex at angle $\theta_1$ to the hinge, which equals $\arctan|(x_2 - x_1)/(y_2 - y_2)|$; on the other side of vertex 2, the fold line angle $\theta_2$ is found using Eqn 1. This line then meets the parabola at the position of the third vertex, whose linked hinges are similarly constructed; for the $i^{\text{th}}$ vertex, $\gamma_i = \pi/2 - \arctan(x_i/2a)$ and $\theta_{i+1} = 2\gamma_i - \theta_i$. The density of hinge lines is controlled by the initial separation between the first two cylindrical hinges but fine-tuned so that the final vertex coincides with the rim. The pattern is then reflected about the $y$ axis.

The spherical image for the $i^{\text{th}}$ vertex is given in Fig. 6(b), where $\beta_i$ are the equal rotations of the fold lines, and for the linked hinges, $\rho_i$. Simple trigonometry gives the ratio as:

$$\frac{\rho_i}{\beta_i} = \frac{\sin(\theta_i - \theta_{i+1})}{\sin\theta_{i+1} + \sin\theta_i} \tag{3}$$

and we construct the complete image set for an example of seven pairs of hinge lines in Fig. 6(c): the facets can be tracked by the labels $\mathrm{C}_1$, $\mathrm{D}_1$ ... to their image positions $\mathrm{c}_1$, $\mathrm{d}_1$ *etc.* The more detailed pattern and images for an arbitrary 47 pairs of hinges is given in Fig. 6(d) along with Eqn 3 plotted against $x/R$. This ratio appears constant, and since $\beta_i$ is the same for Case II patterns, all hinge line rotations are the same. This is a surprising but welcome property which, however, defies a closed-form expression; but because the hinge lines are not evenly spaced, the cylindrical curvature for the buckled part is not uniform—a more interesting outcome. If we also change the density of hinges, the value of $\rho_i$ changes, but for a given parabola and density, it is the same value throughout.

The spherical images in Fig. 6 are, in fact, superficially similar to those of Farmer and Calladine [2]. If our hinge line pattern represents the deformed shape of a continuous (and buckled) plate, the conical portion must remain in contact with the rim during loading, which are points underneath its hinge lines. When these points are connected by straight lines, Fig. 7(a), we have the proposed directions of the rotation vectors about the rim for each conical facet. They can be appended to their corresponding facet points $\mathrm{d}_1$, $\mathrm{d}_2$ ... in Fig. 7(b) where clearly none of them intersect at the same point, which must lie on the symmetry axis shown. In other words, these rotation vectors do not lie in the same plane and the conical section is not everywhere in contact with the (planar) rim. In practice, the discrete conical section sits on its three lowest points, which are difficult to distinguish as there is some elastic deformation of the thin paper card when pressed onto the rim, but it is clear in Fig. 7(c) that the disk edge deviates from planarity, particularly towards the parabolic fold. The optics analogy therefore captures the essence of the deformed shape but it does not comply with the boundary conditions exactly; and we must be mindful of this when employing the special cases here in other problems.

Farmer and Calladine ensure co-planarity by making these edge rotation vectors meet at the same point, which is located from the first spherical image of the central vertex. This image also locates the vertical line along which points $\mathrm{c}_1$, $\mathrm{c}_2$ ... lie; moving along the fold, successive images are constructed of similar shape to Fig. 5 but which do not obey Eqn 1 because of the edge condition. Even though all of their conical-section hinges converge to the same point, it is not at the focus of the parabola but located one-fifth of the radius from its centre, approximately 2.2% differently. The pattern does not strictly conform to Case II and therefore the fold angle varies slightly along its length, and must do to ensure that geometrical compatibility throughout, which includes the boundary conditions, of this intriguing problem are satisfied.

In closing this section, we note that others have approximated the d-Cone shape by two intersecting conical regions of conjoined apices at the point of application of loading: one cone points upwards as the buckled part, and the other downwards. The shape around the loading point is now less refined compared to empirical observations but in return, its variation in terms of each cone's straight-line generators is only circumferential. This gives a simpler shape description but it leads to infinite curvature precisely at the loading point, and thus to infinite strain energy in theory. Such singular behaviour is avoided when we use a parabolic crease: it may even be why it forms in practice. Quite simply, the apex of our conical section is the focus of the parabolic curve, which is a *virtual* point. There is no asymptotic concentration of curvature and any assessment of the equivalent strain energy stored in the d-Cone overall will produce a finite amount. This may be an interesting avenue to explore in view of mechanics of deformation and the natural extent of the d-Cone buckle, which has also occupied researchers.

# 5 Conclusions

We have shown that the generator performance for two cases of inextensible folding about a single curved path first postulated by Duncan and Duncan [1] over thirty years ago can be predicted graphically using Gauss's spherical image construction. The fold curve is rendered piece-wise linear between linked pairs of hinge lines, in order to create a series of foldable vertices. The rotation vectors at each vertex have a unique relationship for developable folding, which can be extrapolated along the fold in successive spherical images. When the hinge pairs are parallel to each other, each spherical image is antisymmetrical and collocated about its centre, resulting in a planar folded curve. When they make equal angles to the local tangent of the curve, each spherical image is symmetrical giving no change in the fold angle between vertices provided the fold line segments between them are also equally inclined to the tangent. Under these presumed fold curve conditions, we may quickly assess the shape of a folded sheet by ensuring that hinge- and fold lines are drawn accordingly. We can extend this to the conception and design of novel folding schemes in a variety of engineering disciplines, from sheet-metal folding to origami inspired shape-changing structures, and beyond in the sense of the underlying principles. For example, it would be interesting to consider multiple fold curves in a single sheet and the interaction of generator patterns between them for compatible folding overall. We also believe our findings hold for large rotations that we hope to confirm in future study.

# References


[1] J P Duncan and J L Duncan. Folded developables. *Proceedings of the Royal Society of London, A*, 383(1784): 191-205, 1982.

[2] S M Farmer and C R Calladine. Geometry of "developable cones". *International Journal of Mechanical Sciences*, 47: 509-520, 2005.

[3] C R Calladine. Theory of Shell Structures. Cambridge University Press, 1983.

[4] J T Bruton, T G Nelson, T K Zimmerman, J D Fernelius, S P Magleby and L L Howell. Packing and deploying soft origami to and from cylindrical volumes with application to automotive airbags. *Royal Society Open Science*, 3: 160429, 2016.

[5] K A Seffen. Compliant shell mechanisms. *Philosophical Transactions of the Royal Society, A*, 370: 2010-2016, 2012.

[6] M A Dias and C D Santangelo. The shape and mechanics of curved-fold origami structures. Europhysics Letters, 100(5): 54005, 2012.

[7] M A Dias, L H Dudte, L Mahadevan and C D Santangelo. Geometric mechanics of curved crease origami. *Physical Review Letters*, 109: 114301, 2012.

[8] F Lechenault, B Thiria and M Adda-Bedia. Mechanical response of a creased sheet. *Physical Review Letters*, 112: 244301, 2014.

[9] M G Walker and K A Seffen. Localization in thin metallic annuli due to diametrical extension. *AIAA Journal*, 55: 3980-3989, 2017.

[10] E Cerda and L Mahadevan. Conical surfaces and crescent singularities in crumpled sheets. *Physical Review Letters*, 80(11): 2358-2361, 1998.

[11] S Chaieb and F Melo. Crescent singularities and stress focussing in a buckled thin sheet: mechanics of developable cones. *Physical Review E*, 60(5): 6091-6103.

[12] T Liang and T A Witten. Crescent singularities in crumpled sheets. *Physical Review E*, 71: 016612, 2005.

## Figures

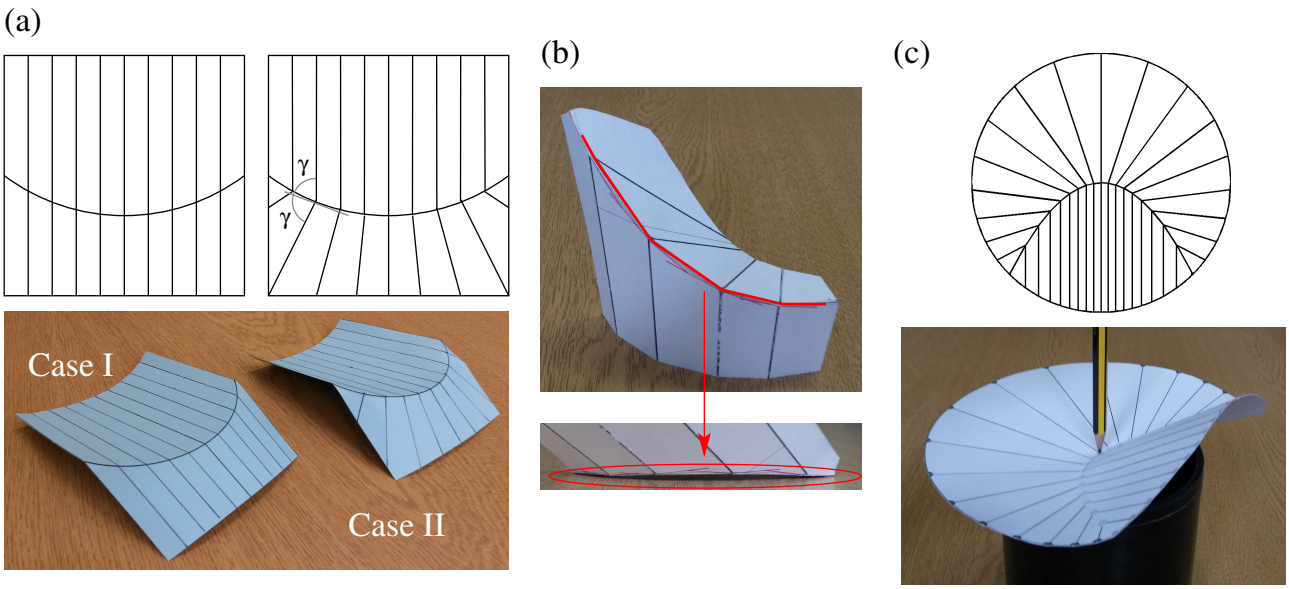


Figure 1: Inextensible folding of paper card about straight generators and a fold curve. (a) Two special cases of Duncan and Duncan [1] shown in planar development (top) where the pairs of generators on either side of the fold are either collinear or equally inclined to the local tangent (at a representative angle $\gamma$), and curved in opposite senses. The folded ridge in the first case remains planar but not in the second, where the fold angle is constant; the lack of planarity is emphasised in (b) in another example. (c) Generator pattern similar to that used by Farmer and Calladine [2] for inextensible d-Cone deformation of a disk supported on a circular rim and loaded by a central point force. The pattern shares features with the second case in [1] where the conical generators would extrapolate to the focus of the parabolic fold curve on the cylindrical generator side.

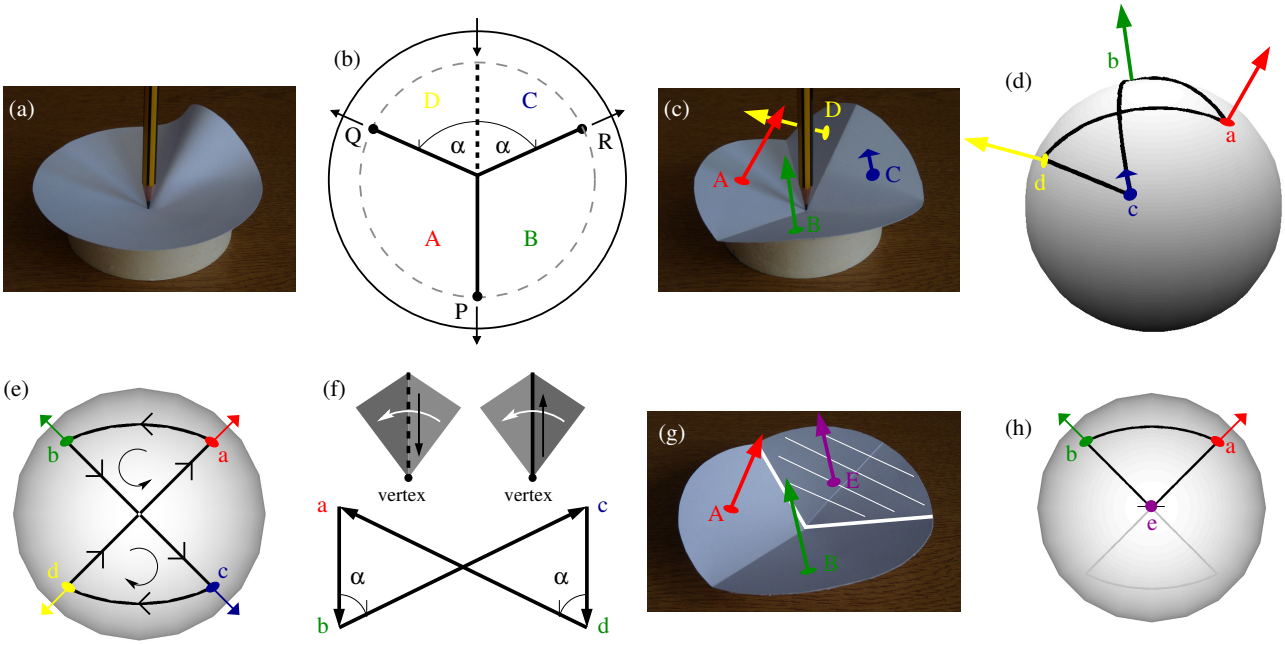


Figure 2: D-Cone formation and description. (a) Original continuous d-Cone; (b) its discretely folded analogue in planar development with three "valley" hinge lines, solid, and a single "mountain" line, dashed, meeting at a central developable vertex. The facets, A, B, C and D are flat and P, Q and R are in contact with points on the support rim (dashed); $2\alpha$ is the angle subtended by the upwards buckle. (c) Normal unit vectors appointed to facets during folding; (d) mapping of normals from (c) onto a sphere of unit radius. Moving between facets around the vertex, A-B-C-D-A, traces out the spherical image of a bow-tie, a-b-c-d-a. (e) Plan view of (d) with equal internal areas in opposite senses. (f) Alternative spherical image from adding hinge line rotation vectors in sequence around the vertex; valley and mountain vectors point away or towards the vertex, respectively, also shown in (b). (g) Replacement of facets C and D by a single planar wedge, E, which borders both valley hinges (white); (h) corresponding spherical image (equal to the top half in (e)).

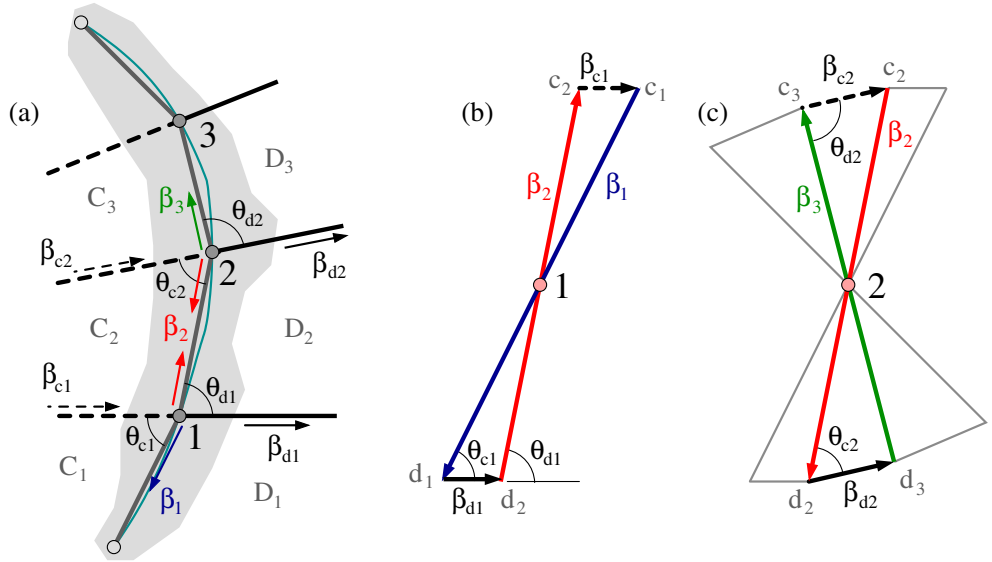


Figure 3: Hinge line analogue of Case I [1] in planar development. (a) Fold curve (cyan/shaded background) discretised by straight line segments (grey) separating vertices 1, 2 *etc.* Linked pairs of collinear hinge lines across the fold at each vertex divide the surface around into four facets: for vertex 1, we have $C_1$, $D_1$, $D_2$ and $C_2$ anticlockwise. Dashed hinges separate facets that rotate in the opposite direction to them separated by solid hinge lines and fold lines: rotation vectors (coloured) accordingly point away or towards the vertex. The layout at vertex 1 is specified by two angles, $\theta_{c1}$ and $\theta_{d1}$, and so forth for vertex 2 .... (b) Spherical image for vertex 1 for small rotations $\beta_1$ and $\beta_2$ of its fold line segments and for $\beta_{c1}$ and $\beta_{d1}$ of its hinge lines. Facets are labelled in lower case and the image has been drawn with equal and opposite areas about the cross-over point. (c) Spherical image for vertex 2, coloured, superposed with that of vertex 1 (grey): the image for vertex 3 has also been added. The cross-over points are the same, indicating that all vertices are co-planar.

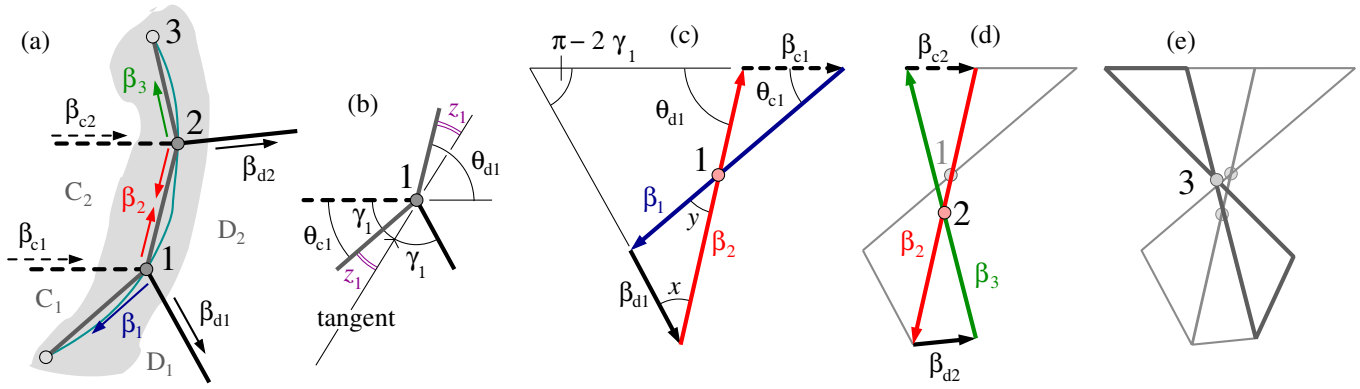


Figure 4: Case II. (a) The labelling scheme follows Fig. 3 and each pair of linked hinge lines at a given vertex make equal angles, $\gamma$, to the local tangent of the original fold: (b) the layout of fold line segments at vertex 1 defined by angles $\theta_{c1}$ and $\theta_{d1}$ measured relative to the dashed hinge. (c) Spherical image for vertex 1 where $x$ and $y$ are auxiliary angles; equal areas sets $\gamma_1 - \theta_{c1} = \theta_{d1} - \gamma_1 = z_1$, giving equally inclined fold line segments in (b), which is repeated for successive vertices; the fold line rotations, $\beta_1$ and $\beta_2$, are the same. (d) Spherical image for vertex 2 of the same fold line rotations but with a different cross-over point, indicating non-planarity of the fold lines. (e) A typical third spherical image.

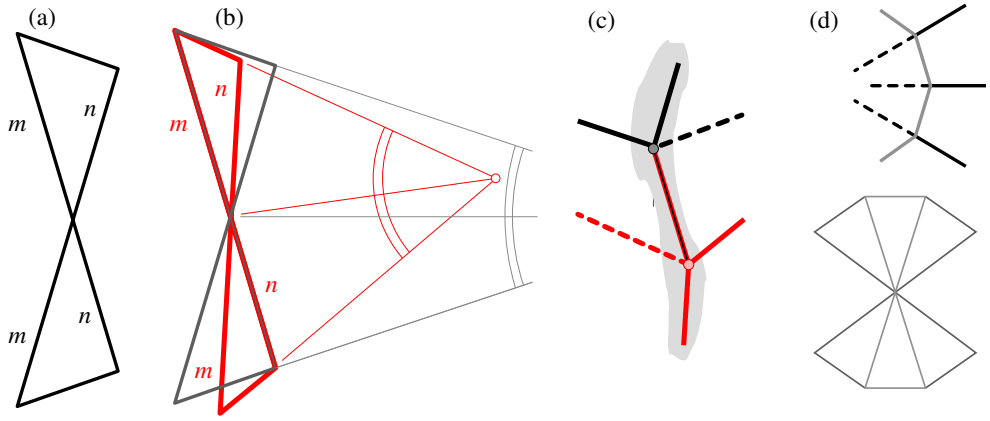


Figure 5: (a) Typical Case II spherical image where the larger, fold line rotations are split into lengths $m$ and $n$ either side of the cross-over point. (b) Spherical image, red, for the next vertex along the fold path, which has the same cross-over point, as well as fold line rotations (by definition from Case II). (c) Reconstruction of the fold line segments (shaded) and hinge lines from the images in (b) where a dashed line is of opposite sense rotation. (d) Top: fold lines (grey) and hinge layout conforming to both Cases I and II and spherical images (bottom) sharing the cross-over point and fold line rotations.

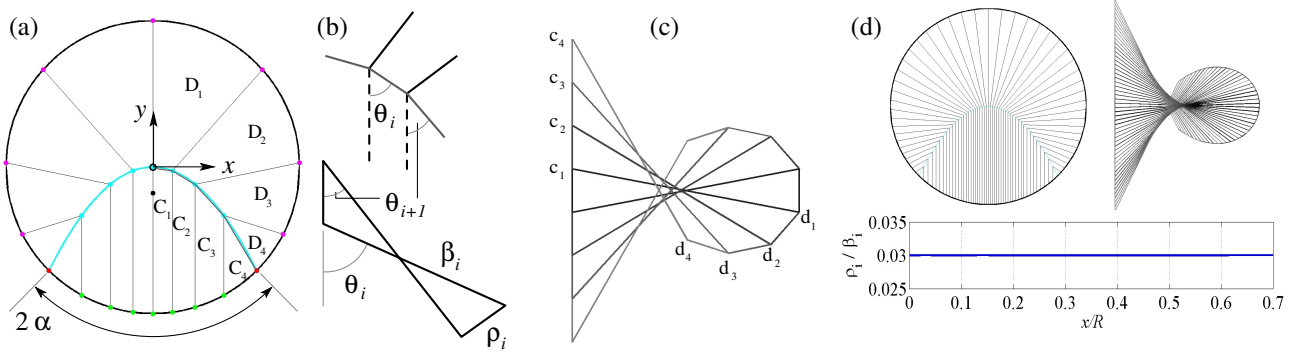


Figure 6: D-Cone shape defined by Case II rules. (a) Initial geometry of seven hinge line pairs with the parabolic fold (cyan) centred on the $(x, y)$ coordinate origin. Facets $C_1 \ldots C_4$ are one half of the cylindrical buckle and $D_1 \ldots D_4$ are for the conical section: coloured points indicate where the hinge lines meet the support rim (assumed to be exactly at the disk edge). (b) Local angle specification for vertex $i$ (for $x > 0$) and its spherical image of rotations $\beta_i$ (fold) and $\rho_i$ (hinge). (c) Spherical images for (a) with $2\alpha = 90°$: facets in the left-hand side are not labelled for simplicity. (d) More detailed pattern of 47 pairs of hinges for the same parabolic fold, their spherical images and the rotation of hinge lines, $\rho_i/\beta_i$.

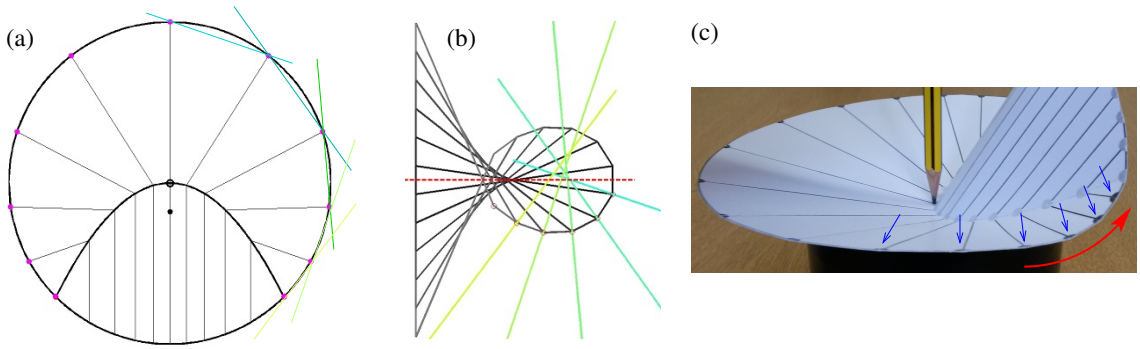


Figure 7: Edge performance of the Case II d-Cone pattern from Fig. 6 (with nine pairs of hinge lines for slightly more detail). (a) Lines of expected rotation vectors of conical facets about support points on the rim. (b) The vectors from (a) appended to the their corresponding spherical images: they all meet the symmetry axis (red) at different points, suggesting that the lines and hence edge points in (a) all lie in different planes. (c) Informal confirmation of (b).